Phantom and Model-Based Near Infrared Spectroscopy Measurements of Intracranial Hematoma From Infants to Adults

Lei Wang, Meltem Izzetoglu, Juan Du, and Hasan Ayaz, *Senior Member, IEEE*

***Abstract*— Hemorrhage is a common consequence of traumatic brain injury and can be detected by near-infrared spectroscopy (NIRS)-based noninvasive sensors over scalp. In this study, our aim was to investigate NIRS measurements comprehensively using both phantoms and simulated head models of different age groups from infant to adult with intracranial hematoma development of various sizes and depths for the first time. Physical phantoms of infant (six-month-old), child (two-year-old), adolescent (12-year-old), and young adult head models with intracranial hematoma of varying sizes and depths were built using a multilayer dynamic phantom and evaluated by an NIRS device. Optically similar models with the same geometric configuration as physical phantoms were developed and used in Monte Carlo (MC) simulations. Optical density (OD) from MC simulations and phantom measurements were compared, and the effect of lesions with varying volumes and locations on photon path were investigated in simulations. Results indicated that phantom measurements and simulated model-based measurements are highly significantly correlated. Presence of the hematoma had a larger effect on light traveling in younger group head models, caused an increase in OD from the healthy state to hematoma development, decrease in distance traveled by the light within the head model, and thus decreased sensitivity of the measurement to the brain layer. The findings of this study can guide the detection and localization of lesions for NIRS-based applications in humans at different ages.**

***Index Terms*— Intracranial hematoma, Monte Carlo (MC) simulation, near infrared spectroscopy (NIRS), physical phantom, traumatic brain injury (TBI).**

I. Introduction

TRAUMATIC brain injury (TBI) refers to the potential for significant injury to the brain parenchyma following head trauma [1]. It is a major public health concern throughout the world [2] and the leading cause of morbidity and disability worldwide, especially in children and young adults [3]. A large portion of survivors of TBI have persistent changes in emotional stability, personality, and independence for activities of daily living, as well as cognitive function [4]. After TBI, intracranial pressure can become elevated due to a combined effect from intracranial hematomas, contusions, and diffuse brain swelling [5]. Intracerebral hemorrhage often occurs in patients with focal head injury [6], and it remains a devastating form of stroke [7]. The initial injury induced by the mechanical effect of the hematoma on surrounding brain tissue as well as the subsequent cascade of processes such as perihematomal edema account for the high 30-day mortality rate and poor neurological outcome in the surviving victims [7]. Detection and monitoring of hemorrhage following TBI may provide additional therapeutic targets, which may potentially be achieved by one or more clinical imaging modalities: near-infrared spectroscopy (NIRS), magnetic resonance imaging (MRI), magnetic resonance spectroscopy (MRS), diffusion tensor imaging (DTI), computed tomography (CT), single-photon emission CT (SPECT), diffuse correlation spectroscopy (DCS), and others [8], [9].

NIRS is an optical technology originally developed for monitoring tissue oxygenation [10], [11]. The physical principles of NIRS are: biological tissues are relatively transparent to light in the near-infrared range, at wavelength of 700–900 nm; the propagation of light through biological tissues depends on reflection, absorption, and scattering [10]; and the main chromophore that contributes to the relatively high attenuation of the light is hemoglobin [11], [12]. Using appropriately placed emitter–detector pairs, NIRS can detect the strength of absorption and scattering across different areas of the brain as NIRS light passes through it [13]. The spatial and temporal dynamics of NIRS allow for the measurement and detection of various intracranial physiological conditions and parameters, which can be utilized to help clinicians in treating patients with TBI [13].

The possibility to detect changes in cortical oxygenation during hyperventilation by NIRS was demonstrated in 1977 on adults [14]. Following that, the first NIRS clinical studies on newborns and adult cerebrovascular patients were published in 1985 [13], [15], and a wealth of studies described the use of NIRS in neonates where it has found clinical application since the 1980s [15], [16]. Through the 1990s, reports on the ability of NIRS in detecting intracranial hematomas marked the beginning of clinical application of NIRS for TBI [13], [17], [18]. Multiple further studies have been performed in localization and detection of intracranial hemorrhage with NIRS, and it was concluded that NIRS

Manuscript received October 21, 2021; revised February 5, 2022; accepted February 24, 2022. Date of publication March 8, 2022; date of current version March 22, 2022. The Associate Editor coordinating the review process was Dr. Kamel Haddadi. *(Corresponding authors: Lei Wang; Meltem Izzetoglu; Hasan Ayaz.)*

Lei Wang is with the Department of Information Science, Drexel University, Philadelphia, PA 19104 USA (e-mail: lw474@drexel.edu).

Meltem Izzetoglu is with the Department of Electrical and Computer Engineering, Villanova University, Villanova, PA 19085 USA (e-mail: meltem.izzetoglu@villanova.edu).

Juan Du and Hasan Ayaz are with the School of Biomedical Engineering, Science and Health Systems, Drexel University, Philadelphia, PA 19104 USA (e-mail: hasan.ayaz@drexel.edu).

Digital Object Identifier 10.1109/TIM.2022.3157343

could detect intracerebral, subdural, and epidural hematomas in a delayed manner following TBI successfully [13], [19]. However, the limited sensitivity of the device and inability to provide anatomic localization of hematomas significantly limit its utility in comparison with the gold standard of a CT scan [13].

Understanding and modeling of light tissue interaction related to the detection of intracranial hematomas is critical for developing next-generation NIRS systems. Monte Carlo (MC) simulation is a computational method which is often applied to model photon migration inside human tissue [20]. Since it effectively solves the radiative transfer equation (RTE) via random sampling, it offers excellent accuracy when simulating photon propagation inside a complex medium [20]. In many cases, MC was chosen as the gold standard when validating a new algorithm or approximation [20], [21]. MC simulation can model how photons travel through different tissue layers, under dynamically and spatially changing conditions for various NIRS instrumentations, and source-detector (SD) types and locations, which are more flexible and informative than physical testing [22]. To the best of our knowledge, MC has been extensively used in the study of healthy human heads of different age groups [23], [24], but not widely and fully explored for clinical applications involving mass lesion development such as intracranial hematomas [8].

Optical phantoms are commonly used as an initial benchmark test for new NIRS devices before they are used in human testing [25], which can serve as a guide to that testing. Measurements obtained from models used in MC simulations and physical laboratory phantoms together can provide a more involved evaluation of the NIRS system in aiding the clinical tests on humans. Together these physical and simulated models can be used for the study of various age groups where data collection in large clinical tests can be hard to conduct. However, there is only a limited number of reports using these two measurements together [26], [27]. To the best of our knowledge, no prior work exists for the study of brain injury conditions such as hematoma development in different age groups using phantom and model-based measurements to investigate light tissue interaction and the outcome intensity measurements from actual NIRS devices.

In this study, our aim was to investigate near-infrared light propagation and outcome intensity measurements related to intracranial hematoma development of various sizes and depths within head models of different age groups. We first built physical phantoms of infant (six-month-old), child (two-year-old), adolescent (12-year-old) and young adult head models with intracranial hematoma of varying sizes and depths. Optical density (OD) values were measured from physical phantoms with a NIRS-based handheld hematoma detector, namely Infrascanner[1] model 2000 ($\lambda = 808$ nm) [9]. Then, MC simulated models with the same geometric configuration as physical phantoms were developed. Optical properties of each tissue measured from physical phantoms were applied in MC simulations. Detector fiber radius and SD separation were selected the same as Infrascanner, model 2000 in MC simulations. In addition to OD, mean total optical pathlength (MPL), transit time, and proportional sensitivity to brain and spatial sensitivity profile were assessed from MC simulations. Combination of the physical phantom measurements and MC simulation measurements provided more complete, in-depth information about the capability of NIRS in intracranial hematoma detection after TBI for different age groups.

[1]Trademarked.

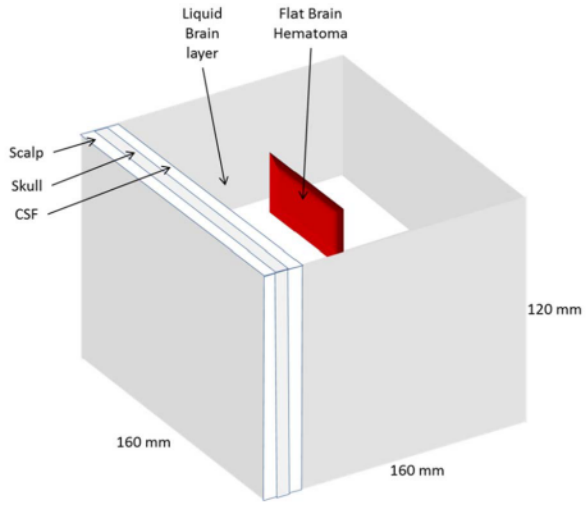

Fig. 1. Scheme of the laboratory mixed multilayered solid and liquid optical brain hematoma model.

II. Methods

A. Phantom Measurement

Physical phantoms were built in the Optical Brain Imaging lab at Drexel University, as a cubic container with an open top as shown in Fig. 1 [28]. Each sidewall of the phantom modeled the extracerebral layers of the human head for one of the four preselected age groups, where the inside of the container was used to model the brain layer. Sidewalls were built as solid phantoms in three layers sequentially from outer to inner layers mimicking the scalp, skull, and cerebrospinal fluid (CSF). Solid phantom layers were made by mixing a silicone material (RTV12A as the base compound and RTV12C as the curing agent), Carbon Black (absorbing agent) and Titanium Dioxide (TiO_2, scattering agent) in appropriate amounts to achieve the optical properties and thicknesses of the intended head layer [29]. The absorption and scattering coefficients of each superficial, solid phantom layer were measured using a frequency domain NIRS system [30] while building the phantom as provided in Table I. Geometric configuration of each side in terms of its selected layer thicknesses representing different age group head models was as shown in Table II [31], [32].

Intralipid, water, and ink solution of appropriate proportions was used in the center of the cubic container to mimic the optical properties of human brain tissue with $\mu a = 0.1$ cm^{-1} and $\mu s' = 5$ cm^{-1} [28], [33], [34]. Sheep whole blood was used in flat containers to mimic hematoma with measured optical properties as $\mu a = 7.2$ cm^{-1} and $\mu s' = 6.49$ cm^{-1}. Lesions were modeled as cuboids, and presented within the brain tissue layer, on the midline between source and detector, in varying volumes: 3, 5, 10, 30, and 50 cm^3. Geometric configuration of hematoma in different volumes were as displayed

TABLE I
TISSUE OPTICAL PROPERTIES IN PHYSICAL HEAD MODELS

		Scalp	Skull	CSF	Brain	Hematoma
Adult	μ_a [/cm]	0.0905	0.0802	0.0388	0.1	7.2
	μ_s' [/cm]	11.02	13.06	1.06	5	6.49
Adolescent	μ_a [/cm]	0.0908	0.0807	0.0388	0.1	7.2
	μ_s' [/cm]	10.9	13.03	1.06	5	6.49
Child	μ_a [/cm]	0.0901	0.0794	0.0388	0.1	7.2
	μ_s' [/cm]	11.05	13.07	1.06	5	6.49
Infant	μ_a [/cm]	0.0901	0.0798	0.0388	0.1	7.2
	μ_s' [/cm]	11.1	13.09	1.06	5	6.49

TABLE II
THICKNESS OF EACH LAYER ON FOUR SIDES OF THE PHANTOM FOR DIFFERENT AGE GROUP MODELS

	Scalp [mm]	Skull [mm]	CSF [mm]
Adult	3	7	2
Adolescent	2.9	6	2
Child	2.5	4	2
Infant	2	2.5	2

TABLE III
VOLUMES AND GEOMETRIC CONFIGURATION OF HEMATOMA MODELS

Lesion size [cm3]	Length [mm]	Width [mm]	Thickness [mm]
3	30	30	3.33
5	40	30	4.17
10	50	40	5.00
30	60	50	10.00
50	80	60	10.42

in Table III, where length of the lesion was kept parallel to SD line. To investigate the ability of NIRS in detecting a lesion at certain depths, the hematoma model was placed at different depths within the brain layer: 0, 10, 20, and 30 mm away from the CSF layer. Detailed fabrication of the physical phantom can be found in [28].

We used a commercially available NIRS-based imaging device developed for hematoma detection, namely Infrascanner model 2000 (Infrascan, Inc.), to obtain measurements from the physical phantoms [9], [35]. The lightweight, hand-held, and battery-operated Infrascanner, model 2000 is designed for rapid hematoma detection in a portable and accurate way that would be ideal for remote locations. The device has an

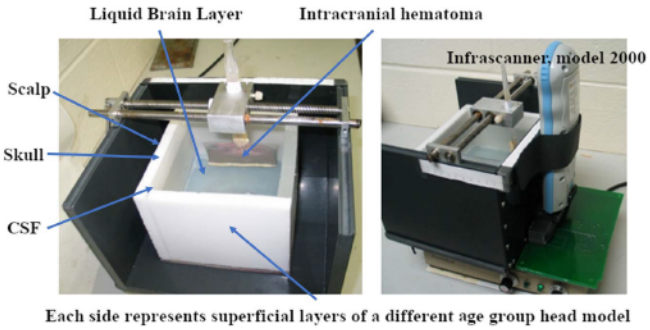

Fig. 2. Laboratory solid/liquid brain hematoma model positioned within a dedicated frame to support the sensors and the hematoma model fastened to a sliding rail (left). Infrascanner Model 2000 positioned during laboratory tests (right).

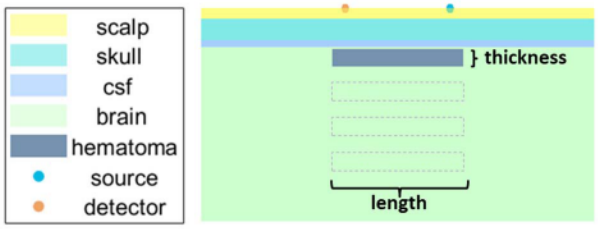

Fig. 3. Geometry of clinical head models for MC simulations.

eye-safe laser diode at 808 nm wavelength and an optical detector at SD separation of 40 mm. The NIRS sensor is placed successively on predefined locations on the left and right frontal, temporal, parietal, and occipital areas of the head and the absorbance of light at selected wavelength is recorded. Decision on hematoma presence is achieved by comparing the difference in OD (ΔOD) from the contralateral sides of the head with a preset threshold value for each head region separately. Physical phantom measurement set up used in this study is shown in Fig. 2. For phantom measurements, there were 40 repeated measurements for each separate model with or without hematoma from each side of the phantom.

B. Model-Based Measurement

3-D models were designed to monitor human heads of four different age groups with intracranial hematoma of different sizes at various depths as illustrated in Fig. 3. Geometric configuration and optical properties of the models were selected the to be same as physical phantoms as provided in Tables I–III. For each age group, a head model for healthy setting without the presence of hematoma was also created and simulated as baseline. Therefore, there were 5 $\times$ 4 (volume $\times$ depth) models for hematoma development and one model for healthy setting per four age groups, resulting in a total of 84 independent head models created.

The Mesh-based MC (MMC) method was adopted for MC simulation, based on the code described by Fang [36], with the general approach described by Wang *et al.* [37]. MMC utilizes a tetrahedral mesh to model a complex anatomical structure. Optical properties assigned to each tissue type for MC simulation were adopted from the physical phantom

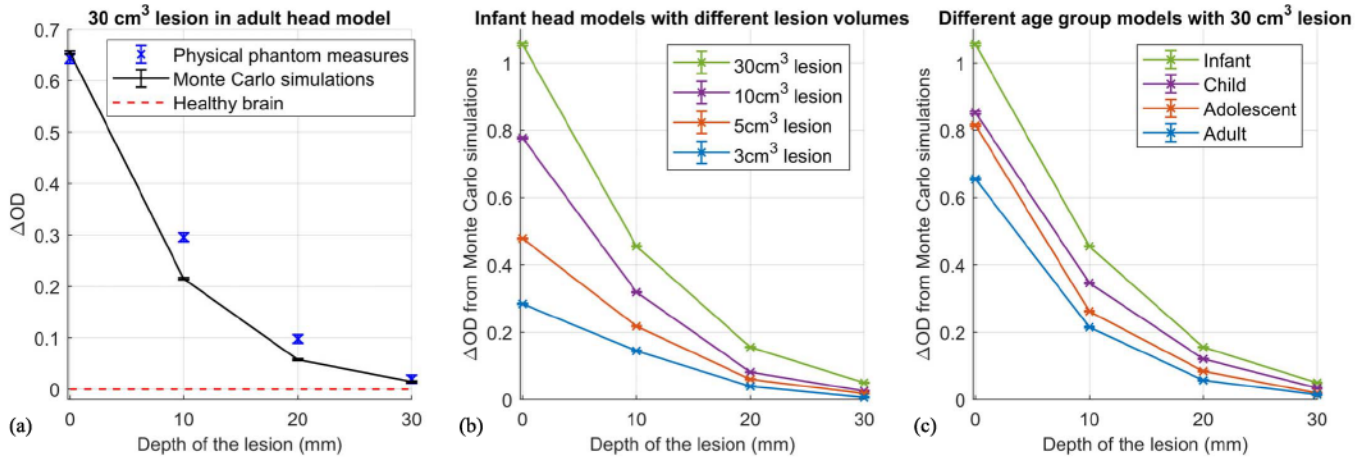

Fig. 4. (a) Mean ΔOD values from phantom and model-based measurements with 30 cm^3 lesion in adult head models, error bar represented standard deviation of 40 measurements. (b) Mean ΔOD values with different lesion volumes (3, 5, 10, and 30 cm^3) from model-based measurements in infants head models, error bar represented standard deviation of 40 measurements. (c) Mean ΔOD values at different age groups (infant, child, adolescent, and adult) with 30 cm^3 lesion from model-based measurements, error bar represented standard deviation of 40 measurements.

values measured by a frequency domain NIRS system [30], as shown in Table I [31], [38]. Light detectors were modeled as a disk with a radius of 0.75 mm, SD separation as 40 mm, which are the same as the configuration of Infrascanner, model 2000 [22]. For each independent head model, there were 40 random simulations where 100 million photons were launched from incident light per simulation. A total of 3360 simulations were run on the hardware supported by Drexel's University Research Computing Facility. The high-performance computer cluster houses both Advanced Micro Devices (AMD) and Intel CPUs with Quad Dara Rate (QDR) Infiniband interconnects and runs the Read Hat Enterprise Linus operating system. As tetrahedral mesh generated noise within MC simulations, no extra noise was added to the simulated results.

In MC simulation, the received intensity of any given photon is attenuated by a factor of $\exp(-\mu_{ai} L_i)$ for any nonzero attenuation in tissue i, where μ_{ai} is the absorption coefficient of tissue i, L_i is the pathlength traveled by single output photon within tissue i, and is calculated by accumulating the scattering length in each medium. Thus, the weight W^j of an exit photon j is found as

$$W^j = W_0 \prod_i \exp\left(-\mu_{ai} L_i^j\right) \tag{1}$$

where initial survival weight W_0 is set to 1 and initial position and direction of a photon are defined as coming from a point source [39], [40]. With a large number of photons captured by detector, the partial differential pathlength (PPL) of layer i is calculated as [39]

$$\mathrm{PPL}_i = \sum_j \left(L_i^j W^j\right) / \sum_j W^j. \tag{2}$$

PPL_i represents the absolute sensitivity to an absorption change in tissue layer i [41]. Then the MPL can be obtained by

$$\mathrm{MPL} = \sum_i \mathrm{PPL}_i. \tag{3}$$

Given MPL and PPL_i, the relative sensitivity, which is the proportion of the total NIRS signal change that derives from a given layer can be defined as follows [32], [41]:

$$\text{Proportional Sensitivity} = \mathrm{PPL}_i / \mathrm{MPL}. \tag{4}$$

III. Results

A. Measured OD

Difference in OD ΔOD under injured conditions (injured brain: hematoma presents in the brain layer) as compared to healthy brain (baseline without the presence of hematoma) is obtained by: $\Delta\mathrm{OD}_{\mathrm{injured}} = \mathrm{OD}_{\mathrm{injured}} - \mathrm{OD}_{\mathrm{healthy}}$.

1) Phantom and Model Comparison: In general, the phantom measurements and model-based measurements are highly correlated (For each age group, with the same lesion volume, Pearson correlation coefficients range from 0.977 to 0.998, $p < 0.05$). Average ΔOD values measured from physical phantoms versus the ΔOD values calculated from the models [22], [32] for 30 cm^3 hematomas at different depths within the brain layer: 0, 10, 20, 30 mm in adult head model are as shown in Fig. 4(a). Each point is the average from 40 phantom measurements or 40 MC simulated measurements. Both phantom measurements and model-based measurements indicated that there is an OD difference between the healthy brain and injured brain when the SD separation is 40 mm [8], [42], [43].

2) Lesion Depth Effect: In Fig. 4(a), average ΔOD values for the same volume (30 cm^3) of the lesion placed at different depths in comparison to healthy brain (the baseline, no hematoma condition, averaged $\Delta\mathrm{OD}_{\mathrm{healthy}} = 0$). As the lesion presented deeper into the brain, ΔOD values decreased in both measurements, gradually getting closer to baseline: $\Delta\mathrm{OD}_{0\,\mathrm{mm}} > \Delta\mathrm{OD}_{10\,\mathrm{mm}} > \Delta\mathrm{OD}_{20\,\mathrm{mm}} > \Delta\mathrm{OD}_{30\,\mathrm{mm}} > 0$.

3) Lesion Volume Effect: When lesion was at the same depth within brain layer, the larger the volume of the lesion, the higher the ΔOD: $\Delta\mathrm{OD}_{50\,\mathrm{cm}\,3} > \Delta\mathrm{OD}_{30\,\mathrm{cm}\,3} > \Delta\mathrm{OD}_{10\,\mathrm{cm}\,3} > \Delta\mathrm{OD}_{5\,\mathrm{cm}\,3} > \Delta\mathrm{OD}_{3\,\mathrm{cm}\,3} > 0$. Results from infant head models are presented in Fig. 4(b).

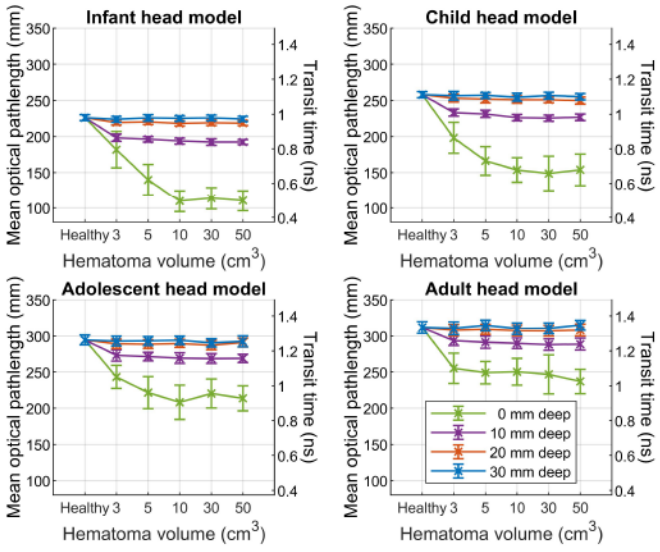

Fig. 5. Mean transit time and corresponding MPL as a function of hematoma volume predicted by MC. Error bar represented standard deviation of 40 random simulations. Each panel represents model for a different age group.

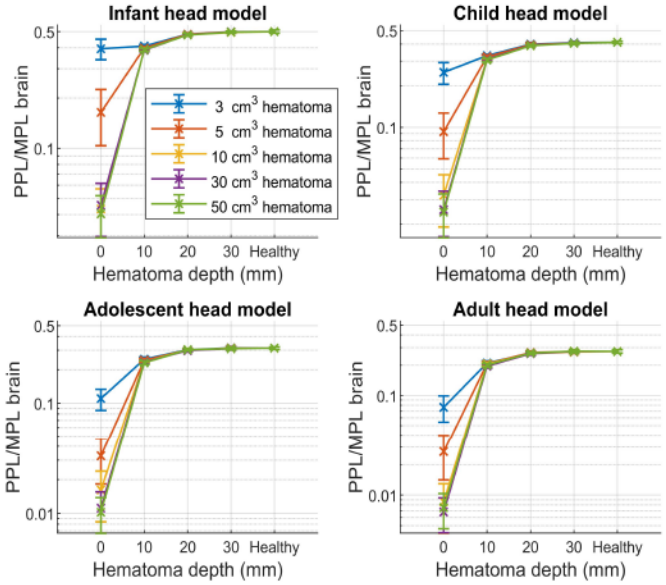

Fig. 6. Mean proportional sensitivity to brain for injured head models as a function of depth lesion presented in the brain predicted by MC simulation. Error bar represented standard deviation of 40 random simulations. Each panel represents model for a different age group.

4) Age Group Effect: When the lesion of the same volume was placed at the same depth within the brain layer, ΔOD values decreased from infant to adult: $\Delta OD_{infant} > \Delta OD_{child} > \Delta OD_{adolescent} > \Delta OD_{adult}$, as shown in Fig. 4(c) for 30 cm^3 lesion in brain. Please note that the plots in Fig. 4(a)–(c) provide mean $\pm$ standard deviation of the ΔOD values where in each case the standard deviations were at least an order of magnitude smaller than the mean value and hence are not visually visible.

B. Mean Total Optical Pathlength

MPL as predicted by MC simulation from 84 head models are shown in Fig. 5. The corresponding mean transit time, which is the meantime taken for the detected light to travel in the tissue [23], is also presented in the figure. With hematoma present in the brain layer, light traveled relatively shorter distances than healthy conditions. This shorter distance was more pronounced when hematoma was closer to the superficial layer. For each curve in Fig. 5, with increased volumes of hematoma, the average distance light traveled was shorter. Curves went flatter when hematoma volumes were greater than 10 cm^3. From infant to adult head models, light traveled longer distances with increasing age group.

C. Proportional Sensitivity

Averaged proportional sensitivity to brain layer (brain + intracranial hematoma) are displayed in Fig. 6. Sensitivity to brain is much higher in infant (up to 50%) than adult (up to 28%). Notably, when hematoma was present at 0 mm depth in the brain, the lesion had relatively larger effect on sensitivity to brain than deeper locations. Compared to baseline, models with hematoma displayed decreased proportional sensitivity to brain of about 46% drop when at depth of 0 mm for infant head model, and only about 28% drop for adult head model. As hematoma presented deeper in brain tissue, curves became less separable and gradually collapsed to baseline profile. Sensitivity to brain decreased as volumes of hematoma increased in all age groups, and curves for 30 cm^3 hematoma and 50 cm^3 hematoma almost collapsed.

D. Spatial Sensitivity Profile

The MC simulated spatial sensitivity profiles on injured head models are displayed in Fig. 7. The example cases presented are for the lesion volume of 3 cm^3, presented at different depths in brain: 0, 10, 20, and 30 mm, compared with healthy brain of four age groups. When the lesion was very close to the superficial layers (0 mm), it had the largest effect on light migration. With lesions located deeper in the brain, the effect of the lesion became weaker. The effect of hematoma on sensitivity profile was greater in younger age models than older group models.

IV. Discussion

In this study, we utilized a set of MC simulations on head models, together with counterpart measurements from a NIRS device on physical phantoms. Our aim was to investigate light propagation within the head under the presence of intracerebral lesions of various sizes and depths in different age groups. Physical phantoms and MC simulation head models of the same optical and geometric characteristics within a multilayered slab geometry mimicked four different age groups (infant, child, adolescent, and adult), with intracranial hematomas of various volumes (3, 5, 10, 30, and 50 cm^3) at different depths (0, 10, 20, and 30 mm) within the brain.

A. Phantom Measurement Versus Model-Based Measurement

The high correlation between phantom measurements and simulation measurements indicated that there was consistency

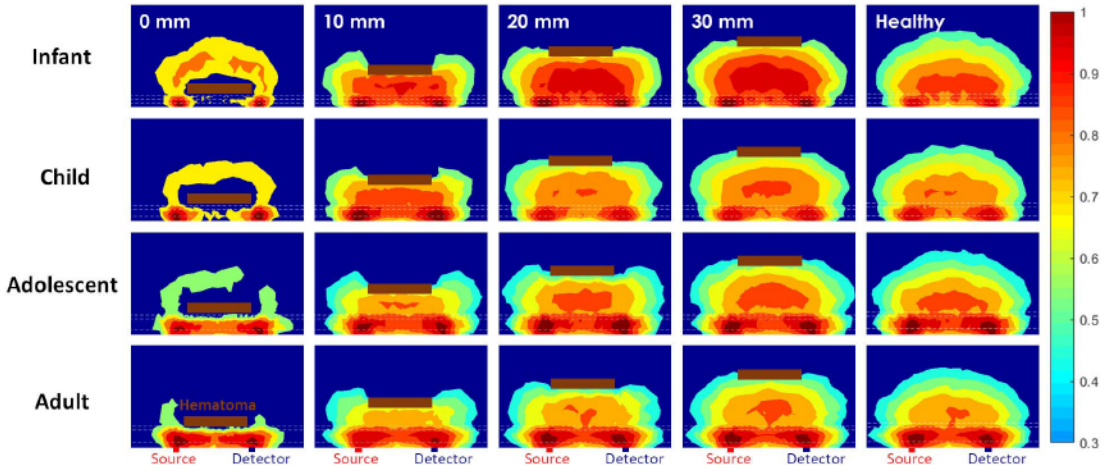

Fig. 7. Spatial sensitivity profile of injured head models (from top to bottom: infant, child, adolescent, adult) with 3 cm^3 lesion presented at different depths in brain layers (from left to right: 0, 10, 20, 30 mm, and healthy head model).

between the two measurements in evaluating lesions of various volumes at different depths. However, there are slight discrepancies between the two measurements as in Fig. 4(a), which could be caused by the following factors: 1) to mimic hematoma, sheep blood was filled in a small container wrapped with rubber (obtained from the cuff part of Diamond Grip™ powder-free examination gloves with thickness of 0.15 mm, which had caused an average drop of 0.0172 in 40 repeated ΔOD measurements of Infrascanner on separate phantom tests conducted in our lab). When the lesion presented at 0 mm deep within the brain layer, the surface of brain layer and hematoma were closely contacted and flat. However, when the lesion presented deeper within the brain layer, such as 10 and 20 mm, the lesion was surrounded by liquid phantom. Due to pressure, the six surfaces of the lesion were not strictly flat as in simulations, which could have resulted in phantom measurements slightly different from model-based measurements; 2) as head models in simulations utilized tetrahedral mesh, throughout the path from source to detector of photons, mesh could have generated noise in model-based measurements leading to the discrepancies between two measurements; and 3) noise that came from the NIRS device itself may have also contributed to the discrepancies between the phantom measurements and model-based measurements. The signal-to-noise ratio (SNR) between the phantom measurements and model-based measurements from each age group model were comparable, as shown in Fig. 8. SNR values were acquired from ΔOD, measured from 21 models for each age group, each model with 40 repeated measurements.

Both phantom and model-based measurements suggested that NIRS could differentiate injured brains from healthy brains. The presence of the hematoma did affect the light path, causing an increase in measured OD, and a decrease in MPL, transit time, and proportional sensitivity to brain. Compared with brain tissue, the relatively higher absorption with hematoma was more pronounced than the slightly higher scattering effect.

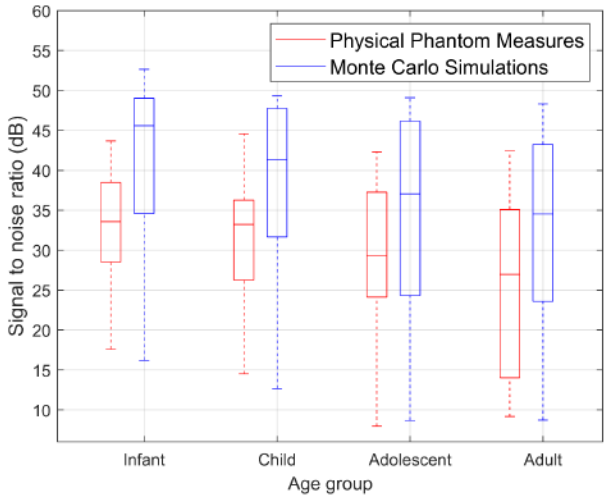

Fig. 8. SNR at different age groups from phantom and model-based measurements, values were acquired from 40 repeated ΔOD measurements from 21 models for each age group.

B. Age Effect

First of all, results demonstrated that age is an important consideration when evaluating the ΔOD values as shown in Fig. 4(c). Future clinical application should consider incorporating age into the evaluation process. Furthermore, there's a monotonic decrease in the ΔOD measurements with increasing age, and hence suggest that age-related contributions can be further modeled for normalization into clinical evaluation.

From adult to infant groups, light traveled shorter distance in shorter time, which validated previous findings about the distance light traveled in older age head models as compared to younger age head models [23]. However, the longer light traveling distance does not imply that a higher portion of measurement came from the brain layer, as indicated by sensitivity measurements from both healthy head models and injured head models (Fig. 6).

The superficial layers (scalp, skull, and CSF) in adult head models are almost twice as thick, and slightly more absorbing and less scattering, than the superficial layers in infant head models. In another aspect, more light gets absorbed in adult head superficial layers, whereas more photons reach the brain layer in infant model which can then reach the light detector. On the other hand, thicker superficial layers enabled the photons to travel longer with more scattering in adult head models. However, even though light travels longer distance in adult models, the received light has more contribution from superficial layers instead of brain layers as compared to infant models.

Measured ΔOD, light traveling distance/time, and sensitivity measures all revealed that intracranial hematoma had a larger effect on light traveling in younger group head models. This is due to differences in layer thicknesses and a higher percentage of the NIRS measurement coming from the brain layer. Such an effect from intracranial hematoma as a function of lesion size or depth in brain follows a logarithmic function rather than a linear one as shown in Figs. 5 and 6.

C. Lesion Effect

1) Lesion Size: With the increase in hematoma volumes, there was an increase in ΔOD. Light traveled a relatively shorter distance in models with relatively larger lesions, and proportional sensitivity of the measured light to brain decreased. The higher absorbing nature of the lesion compared to brain tissue led to more light attenuation by larger lesions, which caused shorter light travel time and relatively smaller contribution to the measurements (proportional sensitivity). Photons that were not absorbed got scattered in the medium around the lesion, and a portion of them made it back to the detector, resulting in higher measured optical intensity.

2) Lesion Depth: As lesions are presented deeper in the brain, measured ΔOD from phantom decreased and got closer to the measurements from healthy head models. This is in line with previous studies on physical phantoms, as the effects of the lesions were stronger when hematoma was closer to the superficial layers than lesions presented deeper in brain [44]. Our simulated measurements were consistent with the findings from physical phantom measurements. They provided a more detailed explanation of the light tissue interaction caused by the lesion. Our findings indicated that the deeper the lesion presented in the brain, the smaller the proportion of the photons got attenuated, with the sensitivity profile gradually getting closer to the profile of healthy models, as were the proportional sensitivity and light travel distance curves. Moreover, these simulated measurements may suggest a potential function of the proposed measures as used in this study versus lesion volume and depth which might be able to provide a reference for future functional NIRS measurements on patients, as well as the detection and localization of lesions.

D. Study Limitation

In this study, we modeled the human head as a layered slab medium in MC simulation, to be the same as the physical phantom. A more complex head structure could be introduced and studied in the future, by considering the true head curvature, spatially varying thickness of extracerebral tissue, and sulci and gyri of the brain tissue. Another limitation of the study is the hematoma model used in MC simulation. We simulated intracranial hematoma in different volumes with a regular rectangular shape of homogeneous structure; however, in real clinical cases, the injured brain may have lesions such as perihematomal edema, cerebral edema, and skin contusions, all of which can be in irregular shapes. These more realistic injury and lesion cases should be investigated in the future, together with skin color and skin contusion effects on light migration.

The optical properties as well as the layer thickness in the study were adopted from previous studies using head models, not directly measured from human tissue *in vivo* [26], [31], [44]–[46]. However, it is well known that there is a natural variation in human head layer thicknesses and optical properties due to age, gender, ethnicity, head location, and other factors [45], [46]. Moreover, there is a wide variety of optical properties and layer thicknesses implemented in the literature and also as measured *in vivo* from human head [26], [28], [40], [44]–[46]. The reported results here investigated one such set of head models and serve as a guidance for actual human subject measurements.

V. Conclusion

In this article, we studied the NIRS measurements of intracranial hematoma models at different sizes and depths in different age groups with a systematic comparison between phantom measurements and model-based measurements for the first time. With the select head models of slab geometry and rectangularly shaped hematoma models as in this study, results suggested that with an SD separation of 40 mm, NIRS could detect hematomas even at 30 mm depth within the brain from OD measurements. Intracranial hematoma could be more easily detected in infant than adult heads due to thinner superficial layers. Lesions with relatively larger volumes would absorb more light-generating larger contrasts to healthy conditions, and hence could be more easily detected than smaller ones. With the presence of intracranial hematoma deeper than 10 mm in the brain, the percentage contribution of the NIRS measurement coming from brain layer cannot distinguish clearly from healthy conditions. The findings in this work are based on the provided head models and hematoma shapes, and hence future studies should investigate the effects of more realistic, curved, and irregularly shaped head and hematoma structures models. The input power of the NIRS device, with comparable photon count in MC simulation together with the effect of mesh size would also be addressed in the future. Nevertheless, the work presented here can help to clarify and emphasize the impact of mass lesion on light-tissue interaction in NIRS measurements using phantom and model-based measurements, which can further aid in the design and evaluation of NIRS-based devices for intracranial hematoma detection.

VI. Disclosures

InfraScan Inc. is the manufacturer of the Infrascanner optical brain monitoring system. Meltem Izzetoglu and

Hasan Ayaz own minor shares at the company due to their contributions to the development of the systems.

ACKNOWLEDGMENT

This work reported here was run on hardware supported by Drexel's University Research Computing Facility. The authors would like to thank Jesse Mark for his help with the article.

REFERENCES

[1] W. Heegaard and M. Biros, "Traumatic brain injury," *Emergency Med. Clinics North Amer.*, vol. 25, no. 3, pp. 655–678, 2007.

[2] E. J. Shiroma, P. L. Ferguson, and E. E. Pickelsimer, "Prevalence of traumatic brain injury in an offender population: A meta-analysis," *J. Correctional Health Care*, vol. 16, no. 2, pp. 147–159, Apr. 2010.

[3] J. Ghajar, "Traumatic brain injury," *Lancet*, vol. 356, no. 9233, pp. 923–929, 2000.

[4] D. J. Schretlen and A. M. Shapiro, "A quantitative review of the effects of traumatic brain injury on cognitive functioning," *Int. Rev. Psychiatry*, vol. 15, no. 4, pp. 341–349, Nov. 2003.

[5] P. J. Hutchinson *et al.*, "Trial of decompressive craniectomy for traumatic intracranial hypertension," *New England J. Med.*, vol. 375, no. 12, pp. 1119–1130, 2016.

[6] D. Lu, A. Mahmood, C. Qu, A. Goussev, M. Lu, and M. Chopp, "Atorvastatin reduction of intracranial hematoma volume in rats subjected to controlled cortical impact," *J. Neurosurgery*, vol. 101, no. 5, pp. 822–825, Nov. 2004.

[7] W. A. Mould *et al.*, "Minimally invasive surgery plus recombinant tissue-type plasminogen activator for intracerebral hemorrhage evacuation decreases perihematomal edema," *Stroke*, vol. 44, no. 3, pp. 627–634, Mar. 2013.

[8] R. Francis, B. Khan, G. Alexandrakis, J. Florence, and D. MacFarlane, "NIR light propagation in a digital head model for traumatic brain injury (TBI)," *Biomed. Opt. Exp.*, vol. 6, no. 9, pp. 3256–3267, 2015.

[9] H. Ayaz, M. Izzetoglu, K. Izzetoglu, B. Onaral, and B. B. Dor, "Early diagnosis of traumatic intracranial hematomas," *J. Biomed. Opt.*, vol. 24, no. 5, 2019, Art. no. 051411.

[10] A. Pellicer and M. del C. Bravo, "Near-infrared spectroscopy: A methodology-focused review," *Seminars Fetal Neonatal Med.*, vol. 16, no. 1, pp. 42–49, Feb. 2011.

[11] H. Ayaz, M. Izzetoglu, K. Izzetoglu, and B. Onaral, "The use of functional near-infrared spectroscopy in neuroergonomics," in *Neuroergonomics*. Amsterdam, The Netherlands: Elsevier, 2019, pp. 17–25.

[12] C. Mu, D. yoon Kim, U. Sunar, K. Pourrezael, and A. Daryoush, "Multi-wavelength NIR system for spectroscopy of biomedical tissues," in *Proc. Int. Topical Meeting Microw. Photon.*, 2003, pp. 275–278.

[13] A. N. Sen, S. P. Gopinath, and C. S. Robertson, "Clinical application of near-infrared spectroscopy in patients with traumatic brain injury: A review of the progress of the field," *Neurophotonics*, vol. 3, no. 3, Apr. 2016, Art. no. 031409.

[14] F. F. Jöbsis, "Noninvasive, infrared monitoring of cerebral and myocardial oxygen sufficiency and circulatory parameters," *Science*, vol. 198, no. 4323, pp. 1264–1267, 1977.

[15] J. E. Brazy, D. V. Lewis, M. H. Mitnick, and F. F. J. vander Vliet, "Noninvasive monitoring of cerebral oxygenation in preterm infants: Preliminary observations," *Pediatrics*, vol. 75, no. 2, p. 217, 1985.

[16] M. Ferrari *et al.*, "Cerebral blood volume and hemoglobin oxygen saturation monitoring in neonatal brain by near IR spectroscopy," in *Oxygen Transport to Tissue VIII*, I. S. Longmuir, Ed. Boston, MA, USA: Springer, 1986, pp. 203–211.

[17] S. P. Gopinath, C. S. Robertson, R. G. Grossman, and B. Chance, "Near-infrared spectroscopic localization of intracranial hematomas," *J. Neurosurgery*, vol. 79, no. 1, pp. 43–47, Jul. 1993.

[18] S. P. Gopinath, C. S. Robertson, C. F. Contant, R. K. Narayan, R. G. Grossman, and B. Chance, "Early detection of delayed traumatic intracranial hematomas using near-infrared spectroscopy," *J. Neurosurgery*, vol. 83, no. 3, pp. 438–444, Sep. 1995.

[19] Y. A. Bozkurt, H. Rosen, A. Rosen, and K. Pourrezaei, "Predicting the onset of intraventricular hemorrhage in premature infants by using functional optical imaging," in *Proc. IEEE 28th Annu. Northeast Bioeng. Conf.*, Apr. 2002, pp. 263–264.

[20] C. Zhu and Q. Liu, "Review of Monte Carlo modeling of light transport in tissues," *J. Biomed. Opt.*, vol. 18, no. 5, May 2013, Art. no. 050902.

[21] V. O. Korhonen *et al.*, "Light propagation in NIR spectroscopy of the human brain," *IEEE J. Sel. Topics Quantum Electron.*, vol. 20, no. 2, pp. 289–298, Mar. 2014.

[22] L. Wang, H. Ayaz, M. Izzetoglu, and B. Onaral, "Evaluation of light detector surface area for functional near infrared spectroscopy," *Comput. Biol. Med.*, vol. 89, pp. 68–75, Oct. 2017.

[23] Y. Fukui, Y. Ajichi, and E. Okada, "Monte Carlo prediction of near-infrared light propagation in realistic adult and neonatal head models," *Appl. Opt.*, vol. 42, no. 16, pp. 2881–2887, 2003.

[24] C. Bonnéry *et al.*, "Changes in diffusion path length with old age in diffuse optical tomography," *J. Biomed. Opt.*, vol. 17, no. 5, 2012, Art. no. 056002.

[25] A. J. Macnab and R. E. Gagnon, "Phantom testing of two clinical spatially-resolved NIRS instruments," *Spectroscopy*, vol. 19, no. 3, pp. 165–169, 2005.

[26] E. Okada, M. Firbank, M. Schweiger, S. R. Arridge, M. Cope, and D. T. Delpy, "Theoretical and experimental investigation of near-infrared light propagation in a model of the adult head," *Appl. Opt.*, vol. 36, no. 1, pp. 21–31, Jan. 1997.

[27] Y. Liu, H. Wang, Y. Liu, W. Li, and Z. Qian, "Monte Carlo and phantom study in the brain edema models," *J. Innov. Opt. Health Sci.*, vol. 10, no. 3, May 2017, Art. no. 1650050.

[28] M. Izzetoglu, J. Du, K. Izzetoglu, H. Ayaz, B. Onaral, and B. B. Dor, "Multilayer, dynamic, mixed solid/liquid human head models for the evaluation of near infrared spectroscopy systems," *IEEE Trans. Instrum. Meas.*, vol. 69, no. 10, pp. 8441–8451, Oct. 2020.

[29] H. J. Juttula, T. P. Kananen, and A. J. Makynen, "Instrument for measurement of optical parameters of turbid media by using diffuse reflectance of laser with oblique incidence angle," *IEEE Trans. Instrum. Meas.*, vol. 63, no. 5, pp. 1301–1309, May 2014.

[30] J. Zhang, *Application of I&Q Detection System in Scouting the Curative Effect of Neck Squamous Cell Carcinoma (Biomedical Optics)*. Bellingham, WA, USA: SPIE, 2003.

[31] A. Demel, K. Feilke, M. Wolf, C. F. Poets, and A. R. Franz, "Correlation between skin, bone, and cerebrospinal fluid layer thickness and optical coefficients measured by multidistance frequency-domain near-infrared spectroscopy in term and preterm infants," *J. Biomed. Opt.*, vol. 19, no. 1, pp. 1–9, 2014.

[32] L. Wang, H. Ayaz, and M. Izzetoglu, "Investigation of the source-detector separation in near infrared spectroscopy for healthy and clinical applications," *J. Biophotonics*, vol. 12, no. 11, Nov. 2019, Art. no. e201900175.

[33] C. C. Sthalekar, Y. Miao, and V. J. Koomson, "Optical characterization of tissue phantoms using a silicon integrated fdNIRS system on chip," *IEEE Trans. Biomed. Circuits Syst.*, vol. 11, no. 2, pp. 279–286, Apr. 2017.

[34] M. Norgia, A. Pesatori, and L. Rovati, "Optical flowmeter for blood extracorporeal circulators," in *Proc. IEEE Intrum. Meas. Technol. Conf.*, May 2009, pp. 1759–1762.

[35] H. Ayaz, B. Ben Dor, D. Solt, and B. Onaral, "Infrascanner: Cost effective, mobile medical imaging system for detecting hemotomas," *J. Med. Devices*, vol. 5, no. 2, Jun. 2011, Art. no. 027540.

[36] Q. Fang, "Mesh-based Monte Carlo method using fast ray-tracing in plücker coordinates," *Biomed. Opt. Exp.*, vol. 1, no. 1, pp. 165–175, 2010.

[37] L. Wang, S. L. Jacques, and L. Zheng, "MCML—Monte Carlo modeling of light transport in multi-layered tissues," *Comput. Methods Programs Biomed.*, vol. 47, no. 2, pp. 131–146, Jul. 1995.

[38] J. Zhao, H. S. Ding, X. L. Hou, C. Le Zhou, and B. Chance, "*In vivo* determination of the optical properties of infant brain using frequency-domain near-infrared spectroscopy," *J. Biomed. Opt.*, vol. 10, no. 2, 2005, Art. no. 024028.

[39] M. Hiraoka *et al.*, "A Monte Carlo investigation of optical pathlength in inhomogeneous tissue and its application to near-infrared spectroscopy," *Phys. Med. Biol.*, vol. 38, no. 12, p. 1859, 1993.

[40] G. E. Strangman, Z. Li, and Q. Zhang, "Depth sensitivity and source-detector separations for near infrared spectroscopy based on the Colin27 brain template," *PLoS ONE*, vol. 8, no. 8, Aug. 2013, Art. no. e66319.

[41] G. E. Strangman, Q. Zhang, and Z. Li, "Scalp and skull influence on near infrared photon propagation in the Colin27 brain template," *NeuroImage*, vol. 85, pp. 136–149, Jan. 2014.

[42] Q. Zhang, H. Y. Ma, S. Nioka, and B. Chance, "Study of near infrared technology for intracranial hematoma detection," *J. Biomed. Opt.*, vol. 5, no. 2, pp. 206–214, 2000.

[43] S. Kahraman, H. Kayali, C. Atabey, F. Acar, and S. Gocmen, "The accuracy of near-infrared spectroscopy in detection of subdural and epidural hematomas," *J. Trauma, Injury, Infection, Crit. Care*, vol. 61, no. 6, pp. 1480–1483, Dec. 2006.

[44] J. Wang, J. Lin, Y. Chen, C. G. Welle, and T. J. Pfefer, "Phantom-based evaluation of near-infrared intracranial hematoma detector performance," *J. Biomed. Opt.*, vol. 24, no. 4, 2019, Art. no. 045001.

[45] M. Izzetoglu, K. Pourrezaei, J. Du, and P. A. Shewokis, "Evaluation of cerebral tissue oximeters using multilayered dynamic head models," *IEEE Trans. Instrum. Meas.*, vol. 70, pp. 1–12, 2021.

[46] Y. Hoshi, M. Shimada, C. Sato, and Y. Iguchi, "Reevaluation of near-infrared light propagation in the adult human head: Implications for functional near-infrared spectroscopy," *J. Biomed. Opt.*, vol. 10, no. 6, 2005, Art. no. 064032.

Lei Wang received the Ph.D. degree in biomedical engineering from Drexel University, Philadelphia, PA, USA, in 2019.

She is an Assistant Teaching Professor with the College of computing and Informatics, Drexel University. Her research focuses on biomedical optical brain imaging, cognitive workload following pediatric concussion.

Meltem Izzetoglu received the Ph.D. degree in electrical and computer engineering from Drexel University, Philadelphia, PA, USA, in 2002.

She is an Assistant Professor in electrical and computer engineering with Villanova University, Villanova, PA, USA. Her research is centered around design, development, and testing of functional near infrared spectroscopy (fNIRS)-based brain imaging systems using laboratory phantoms, animal models and human experimentation, signal processing and algorithm development for artifact cancellation and information extraction. Her research projects involve the application of fNIRS technology for brain activity and physiological monitoring in everyday and everywhere environments as well as in clinics in all age groups from infants to older adults of healthy and disease populations such as traumatic brain injury and multiple sclerosis patients.

Juan Du received the B.S. degree from the Chongqing University of Civil Engineering and Architecture, Chongqing, China, in 1986, where her special focus was on electro-mechanical device installation.

She is a Research Technician with the School of Biomedical Engineering, Science and Health Systems, Drexel University, Philadelphia, PA, USA. Her research is centered around the design, development, and evaluation of tissue simulating phantoms for optical spectroscopy and imaging applications, device development, calibration, and testing.

Hasan Ayaz (Senior Member, IEEE) is an Associate Professor with the School of Biomedical Engineering Science and Health Systems, Drexel University, Philadelphia, PA, USA. His research involves understanding the neural mechanisms related to human cognitive, and motor functioning with a focus on real-world contexts, utilizing mobile neuroimaging, and deploying neuroengineering approaches for neuroergonomics applications. His research aims to design, develop, and utilize next-generation optical brain imaging for neuroergonomic applications over a broad-spectrum including aerospace to health care.